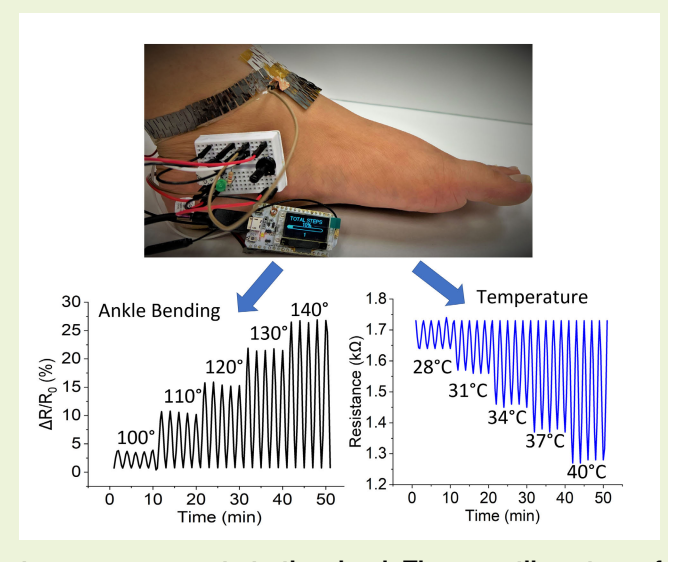


Kirigami-Shaped Dual-Functional Strain and Temperature Sensors for Monitoring Body Movements and Hyperthermia Toward Physiotherapy Applications

Tanzila Noushin¹⁰, Student Member, IEEE, and Shawana Tabassum¹⁰, Member, IEEE

Abstract—Multifunctional sensors find widespread applications in wearable healthcare, Internet of Things (IoT), environmental monitoring, and human-machine interactions, yet they suffer from reduced stretchability, durability, wearability, and enhanced signal crosstalk. This work presents a new kirigami-shaped dual-functional patch that integrates both strain and temperature sensors in a single platform. The kirigami architecture allows out-of-plane deformation of the sensors enabling them to conform to different body parts. The sensing regions are functionalized with gold nanoparticle (AuNP)-decorated multiwalled carbon nanotubes (MWCNTs) that provide highly sensitive and repeatable performance. The strain sensor has a gauge factor (GF) of around 220 at 0.12% bending strain and the temperature sensor shows a sensitivity of 0.0278 k $\Omega \cdot {}^{\circ}C^{-1}$. In addition, the sensor demonstrates an ultrahigh stretchability for an applied tensile strain of up to 180%. The sensors can precisely monitor the dynamic bending of different joints in the body and temperature as well as decouple the strain and temperature measurements in response to dual stimuli. Furthermore, the sensors are interfaced with an IoT platform



that allows wireless transmission of body motion and temperature measurements to the cloud. The versatile nature of the sensing patch holds great promise for continuous monitoring of the progress in physiotherapy so that recovery can be tracked in real time and appropriate intervention measures can be applied.

Index Terms—Kirigami, motion sensing, multifunctional sensing, physiotherapy, strain sensor, temperature sensor.

I. INTRODUCTION

HUMAN motion contains rich physiological information often related to a variety of health problems, including movement disorders, freezing of gait, and muscle aches, which may provide early signs of rheumatoid arthritis, Parkinson's

Manuscript received 20 April 2023; revised 28 April 2023; accepted 29 April 2023. Date of publication 5 May 2023; date of current version 14 March 2024. This work was supported in part by the VentureWell under Grant 21716-20 and in part by the National Science Foundation under Award ECCS2138701. The associate editor coordinating the review of this article and approving it for publication was Prof. Jeong Bong Lee. (Corresponding author: Shawana Tabassum.)

Tanzila Noushin was with the Department of Electrical Engineering, The University of Texas at Tyler, Tyler, TX 75799 USA. She is now with the Department of Electrical and Computer Engineering, The University of Texas at Dallas, Richardson, TX 75080 USA (e-mail: tanzila.noushin@utdallas.edu).

Shawana Tabassum is with the Department of Electrical Engineering, The University of Texas at Tyler, Tyler, TX 75799 USA (e-mail: stabassum@uttyler.edu).

Digital Object Identifier 10.1109/JSEN.2023.3272622

disease, and multiple sclerosis [1], [2], [3]. In addition, long office hours make workers sit for a long period, significantly increasing the risk of back and neck pain [4], [5]. This is particularly prevalent in the postpandemic era in which a hybrid workplace model emerges as a new normal. Moreover, people experiencing ankle sprain or limb surgery are often prescribed physiotherapy that speeds up the recovery process by providing improved mobility and flexibility, restoring strength and function, and minimizing scar tissue development [6], [7], [8], [9], [10]. Ankle and leg fractures are particularly prevalent in athletes and the elderly population [11]. Depending on the severity of the injury and the outcome of surgery, these physical therapy sessions are either guided by a therapist or self-administered. In both cases, it is crucial to continuously monitor the physiotherapy progress so that recovery of the injury can be tracked, and changes can be incorporated into the exercise program accordingly. Lack of monitoring may lead to irreversible secondary injuries. Research shows that

sensor-based long-term monitoring of rehabilitation exercises enables personalized treatment tuned to each patient's recovery trajectory [12]. Hence, real-time monitoring and tracking of various movements and exercise records of people in daily life would enable personalized and just-in-time intervention. Besides physiotherapy, hyperthermia therapy is yet another technique to treat body aches, pains, strains, and sprains [13]. The treatment is often applied in multiple sessions where the temperature needs to be well-controlled in the range of 42 °C-45 °C [14]. Instead of attaching multiple sensing components with a singular modality to the body, a single multifunctional sensor that measures both strain and temperature in a single platform without compromising functionalities compared to conventional devices would provide significant scientific and technological advancement in wearable electronics. Toward this end, a multifunctional wearable sensor that has excellent sensing capability can simultaneously detect both body movements and temperature, can not only decouple multiple stimuli signals but can also decouple motion artifacts from the desired signal, has good stretchability, wearability, and washability, and is interfaced with the Internet-of-Things (IoT) platform, will automate the tracking of body movement and exercise records, and help the patients quickly return to their normal life [15], [16], [17], [18], [19]. Remote monitoring will also allow the clinician to provide telemedicine without the need to be physically present at the patient's location.

Considerable research efforts have been spent on designing multifunctional wearable sensors that monitor various physiological conditions. For instance, zinc oxide nanowires have been used previously to detect both strain and temperature variations [20]. The sensor demonstrated a gauge factor (GF) of 15.2 to strain variations and a sensitivity of 39.3%°C⁻¹ to temperature changes. Bi et al. [21] proposed nickel-carbon nanotubes functionalized fabric as an integrated strain, temperature, and humidity sensor. The sensor showed excellent stability in corrosive environments. However, the aforementioned sensors suffer from signal crosstalk due to the reliance on identical types of electrical signals. To efficiently decouple signals in a multifunctional sensor, Wen et al. [22] developed a highly stretchable, breathable, and self-powered sensor that simultaneously detected tensile strain and temperature. The sensor was fabricated in a multilayered fashion, with a composite layer of thermoplastic polyurethane fibrous membranes functionalized with carbon nanotubes to respond to tensile strain variations and another layer of poly(3.4ethylenedioxythiophene):poly(styrenesulfonate) (PEDOT:PSS) as the temperature-sensitive material. Although the proposed sensor demonstrates superior performance in terms of effective signal decoupling in response to dual stimuli and enables self-powered operation, the sensor is not conformable to different parts or joints of the body. To overcome the skin conformity issue, researchers are exploring the Japanese art of cutting papers, called kirigami, to produce ultrasensitive, highly stretchable, and repeatable wearable sensors. The cuts and notches engraved in a kirigami framework allow in-plane and out-of-plane deformations achieved with a 2-D sheet [23]. Such a shape-morphing characteristic endows superior stretchability and skin compliance under dynamic movements [24], [25]. Kirigami architecture has been used to develop stretchable and tunable solar cells [26], supercapacitors [27], strain-insensitive wearable sensors [28], implantable bioprobes [29], graphene transistors [30], and diffraction gratings [31]. However, more research is needed to uncover the full potential of kirigami structures in wearable sensors and electronics.

This work reports a highly stretchable, kirigami-structured dual-functional sensor that detects strain and temperature stimuli in a single platform. The sensor was cut into a kirigami shape followed by screen printing of conductive electrodes [32] and functionalization of gold nanoparticles (AuNP)-coated multiwalled carbon nanotubes (MWCNT). The kirigami structure allowed skin conformity at different joints in the body along with high sensitivity, repeatability, and washability. In addition, manufacturing the sensor did not require any cleanroom procedures or costly physical operations (i.e., etching, surface cleaning, and surface preparation). Furthermore, the IoT-based interfacing allowed wireless transmission of body motion and temperature measurements to the cloud. To the best of our knowledge, this work reports the first-of-its-kind kirigami-patterned dual-functional smart strain and temperature sensing device that shows versatile performance by measuring body temperature and ankle, wrist, elbow, knee, and neck movements with the same configuration. The sensor will find applications in a variety of fields, including electronic skins [33], environmental monitoring [34], crop health monitoring [35], and human-machine interfaces in robotic systems [36]. The work presented in this article is an extended version of the preliminary results that we presented at the IEEE Sensors Conference 2022 [37]. Here, we discuss the dual functionality of the kirigami structure by integrating both strain and temperature sensors. Also, the dynamic bending of different joints in the body is analyzed and the decoupling of strain and temperature measurements is demonstrated. In summary, the innovative features of this work include the following:

- kirigami-patterned versatile strain and temperature sensor that can morph into an anklet or bracelet or other shapes depending on which joint it is attached to:
- effective decoupling of strain and temperature measurements under dual stimuli;
- measuring dynamic bending of different joints in the body including ankle, wrist, elbow, knee, and neck;
- 4) high sensitivity, repeatability, and washability.

II. SENSOR FABRICATION

A. Fabrication of the Kirigami Framework

A programmable automated cutter (PrismCut, Model P20) from USCutter, Tukwila, WA, USA, was used to carve the cuts and hinges on two different thicknesses (25 and 125 μ m) of flexible polyimide sheets (12 in wide, 12 in long, Amber, Semi-Clear, 16 000 psi Tensile Strength, and Plain, polyimide film, Model BULK-PF-PI-3, Grainger, Lake Forest, IL, USA). According to findings from the literature, strain sensors fabricated with other flexible materials such as polydimethylsiloxane (PDMS) demonstrate a minor variation in resistance even

Authorized licensed use limited to: Iowa State University Library. Downloaded on May 12,2024 at 21:53:58 UTC from IEEE Xplore. Restrictions apply.

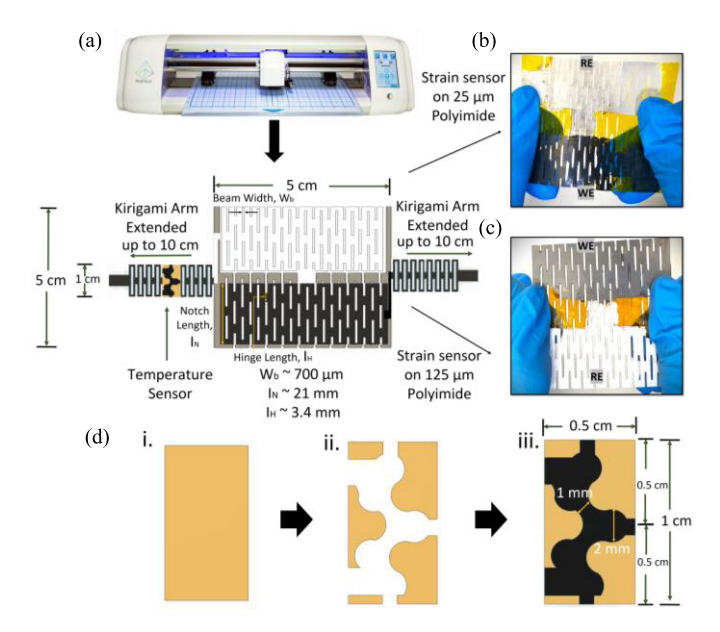


Fig. 1. (a) Kirigami structured sensors fabricated with a programmable cutter where the square-shaped central part is 5×5 cm and arms are extended up to 10 cm long and have a width of 1 cm on each side. Optical images of the strain sensor realized on (b) 25- μ m and (c) 125- μ m flexible polyimide substrates. (d) Fabrication process flow for the temperature sensor: (i) planar polyimide substrate coated with a transfer tape, (ii) programmable cutter transferred preloaded patterns on the taped polyimide substrate followed by the removal of transfer tape from the electrode areas, and (iii) graphene screen-printed on the exposed regions to realize the temperature sensing electrode having an overall dimension of 1×0.5 cm.

under a tensile strain of 430%, thus exhibiting a low GF [38]. In contrast, our sensor shows a larger variation in relative resistance for applied tensile strain up to 180% (explained in Section III-C), thus justifying the use of polyimide as the substrate material.

The design was first made in AutoCAD Fusion 360 and then imported into the programmable cutter. The speed and force of the cutter blade were adjusted at 30 mm/s and 4.75 N, respectively. The cutter then produced kirigami cuts and hinges in the preloaded polyimide sheet. Fig. 1(a) shows the dimensions of the kirigami design, in which the hinge length is 3.4 mm and the beamwidth is 700 μ m for a unit cell. The square-shaped central part is 5 × 5 cm, while the extended arms are 10 cm long and 1 cm wide on each side.

B. Fabrication of the Strain and Temperature Sensors

The strain sensor was fabricated on the square-shaped central part of the kirigami structure. The strain sensor was composed of two electrodes, a working electrode (WE) and a reference electrode (RE). The electrodes were formed using a screen-printing process. The WE was screen-printed with graphene ink (part no. of 805556, procured from Sigma-Aldrich, St. Louis, MO, USA), while the RE was screen-printed with Ag/AgCl paste (part no. of 901773, procured from Sigma-Aldrich). Subsequently, the electrodes were cured at 80 °C for 1 h in a convection oven. Fig. 1(b) and (c) shows the kirigami-structured strain sensing electrodes realized on 25- and 125- μ m-thick polyimide substrates.

The temperature sensor was made on an extended arm of the kirigami structure, as shown in Fig. 1(a), with Fig. 1(b) and (c) illustrating the strain sensor configuration. Fig. 1(d) shows the fabrication process flow for the temperature sensor. A transfer tape was used to cover the polyimide sheet [see Fig. 1(d-i)] followed by producing the electrode patterns with the programmable cutter. Next, the transfer tape is removed from the electrode areas [see Fig. 1(d-ii)]. Subsequently, only the exposed areas were selectively patterned with graphene ink [see Fig. 1(d-iii)] and cured at 80 °C for 1 h. Afterward, the transfer tape was removed so that the electrode patterns were transferred to the polyimide sheet. The overall size of the temperature sensor is 1×0.5 cm. Although the thickness of the graphene electrode cannot be precisely controlled in the screen-printing process, the average electrode thickness can be increased linearly with each added layer [39].

In order to incorporate strain and temperature sensing functionality into the kirigami electrodes, the WE of the strain sensor and the electrode of the temperature sensor were modified with AuNP-embedded MWCNTs mesh [40]. Several strain sensors reported in the literature used CNT and MWCNT nanocomposites as a sensing material due to their tunable electrical conductivity, enhanced mechanical properties, high GF, and excellent piezoresistive or strain sensing properties, thus making the fabricated strain sensors suitable for smart multifunctional textiles and wide sensor arrays [41], [42], [43]. In addition, in our previously reported wearable wound sensor [40], the addition of gold (Au) nanoparticles enhanced the electrical conductivity of the MWCNT nanocomposite. Therefore, to summarize, we used Au-MWCNT nanocomposite in this work due to the tunable electrical conductivity, enhanced mechanical properties, high GF, excellent strain sensing properties of MWCNT, and improved electrical conductivity provided by Au nanoparticles. The preparation steps for the AuNP-MWCNT composite are explained hereafter. First, 0.01% (w/v) tetra chloroauric (III) acid (HAuCl₄·H₂O) (obtained from Sigma-Aldrich) was reduced by 1% (w/v) sodium citrate to prepare the AuNPs using the Turkevich method [see Fig. 2(i) and (ii)] [44]. Separately, 1% (w/v) MWCNT (purchased from ACS Material, LLC, Pasadena, CA, USA) was dissolved in chitosan [see Fig. 2(iii)] and then sonicated for 8 h to prepare the MWCNT suspension solution [see Fig. 2(iv)]. Subsequently, MWCNT dispersion and AuNP solution were mixed in equal volumes [see Fig. 2(v)] and sonicated for 2 h to prepare 1% (w/v) AuNP-MWCNT conjugate. The solution was kept at rest for a day to promote AuNPs integration into the MWCNT network [32]. Finally, 300 μ L of the AuNP-MWCNT solution was loaded in a pipette with a tip diameter of 1.1 mm [see Fig. 2(vi)] and drop-cast on the graphene electrodes [see Fig. 2(vii)] followed by drying at room temperature for 3 h. We used MWCNT as the sensing layer due to its high interfacial bonding with the underlying polymer substrate enabling the sensor to recover its performance upon multiple cycles of stretching/bending and releasing [45]. In addition, the incorporation of AuNPs resulted in improved sensing and stability performance [46]. The electrodes of the strain sensor were passivated with ecoflex coating to prevent crack formation under multiple cycles of

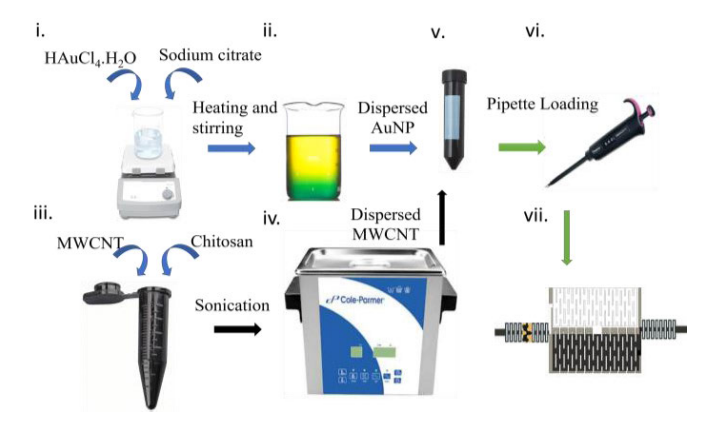


Fig. 2. Schematic illustration of surface modification of graphene electrodes by AuNP-embedded MWCNTs. (i) 0.01% (w/v) HAuCl $_4\cdot H_2O$ was mixed with 1% (w/v) sodium citrate and (ii) stirred and heated to prepare the AuNPs dispersion using the Turkevich method. Separately, 1% (w/v) MWCNT was (iii) dissolved in chitosan and (iv) sonicated for 8 h to prepare the MWCNT suspension solution. (v) Subsequently, MWCNT dispersion and AuNP solution were mixed in equal volumes to prepare 1% (w/v) AuNP-MWCNT conjugate. (vi) Finally, the AuNP-MWCNT solution was loaded in a pipette and (vii) drop-cast on the graphene electrodes followed by drying at room temperature for 3 h.

bending, stretching, or twisting deformations. Although polyimide sheets, graphene, and MWCNTs have inherent flexible characteristics, under a large tensile or bending strain, cracks form in the MWCNT layer (please refer to Section III). The thin ecoflex coating atop the AuNP-MWCNT layer provides an additional protective layer to reduce the crack formation in the underlying MWCNT layer (by distributing the strain in the topmost ecoflex layer) and increasing the operating range of the sensor. In addition, the ecoflex coating protected the skin from coming in direct contact with the active sensing regions and also protected the sensor itself against unwanted touch, contact, or scratches [47].

C. IoT-Enabled Data Acquisition and Processing

We interfaced the kirigami-structured sensors with an IoT-enabled data acquisition and processing unit for real-time and continuous monitoring of body movements and temperature, as shown in Fig. 3(a) and (b).

The data acquisition and processing unit [see Fig. 3(c)] was composed of an ESP32 microcontroller with an inbuilt analog-to-digital converter (ADC) and onboard Wi-Fi module. The resistance variations of the sensors were converted to voltage signals via a voltage divider circuit, which was composed of a known resistor connected in series with the sensor. The output voltage of the voltage divider was sent to the in-built ADC of the ESP32 microcontroller. The microcontroller extracted the bending angle and temperature information by comparing the measured resistance/voltage value with a previously stored calibration curve. Based on the extracted angle, the microcontroller updated the count when proper bending was achieved. The microcontroller sent the count information to an onboard 0.96-in organic lightemitting diode (OLED) display, an LED, and a buzzer. The OLED displayed the step counts and the percentage of a target attained. In addition, the blinking LED and buzzer notified the

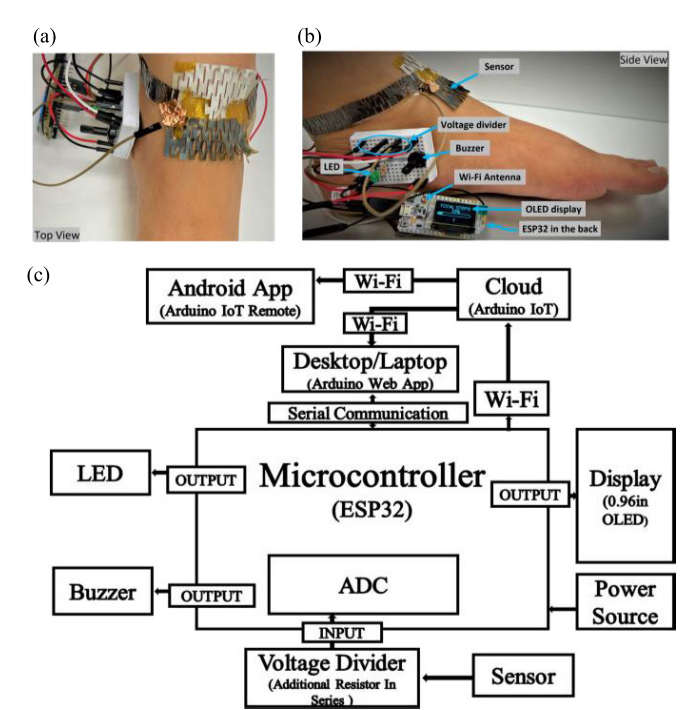


Fig. 3. (a) Top and (b) side views of the sensing system attached around the ankle. (c) Block diagram of the IoT-enabled data acquisition and processing unit. Different components in (c) block diagram are labeled in (b).

patient of his/her physiotherapy progress. The buzzer produced multiple alarms when the exercise session of a body part was completed (for instance, one session could be composed of ten ankle flexes). The information on the bending angle, the number of steps taken, and the completion of a session were uploaded to the cloud via an onboard Wi-Fi module and displayed on a smartphone application. These data could also be transmitted to a desktop/laptop application through serial communication or Wi-Fi communication with the cloud. Such a real-time monitoring system would allow physiotherapists to track injury recovery and prescribe just-in-time interventions.

III. Device Characterization

A. Microscopic and Spectroscopic Analysis

The scanning electron microscopy (SEM) image of the AuNP-decorated MWCNT coating is shown in Fig. 4(a). The SEM image shows the distribution and morphology of the tangled conductive MWCNT structure. The average diameter of the CNTs was found to be 25 nm. The AuNP-MWCNT coating was also characterized by Fourier transform infrared (FTIR) spectroscopy [see Fig. 4(b)]. The absorption peaks between 3500 and 4000 cm⁻¹ were attributed to the -OH functional groups. The peaks in the 1100-1160, 1390-1700, and 2975-3065 cm⁻¹ ranges confirmed the presence of C-H bonds. The broad peaks occurring between 1950 and 2210 cm⁻¹ resulted from the artifacts of the diamond attenuated total reflectance (ATR) setup. One sharp peak was observed at 750 cm⁻¹, which was due to the presence of Au-S bonds in the layer. The FTIR spectrum presented in this article agrees with previous reports [40], [48].

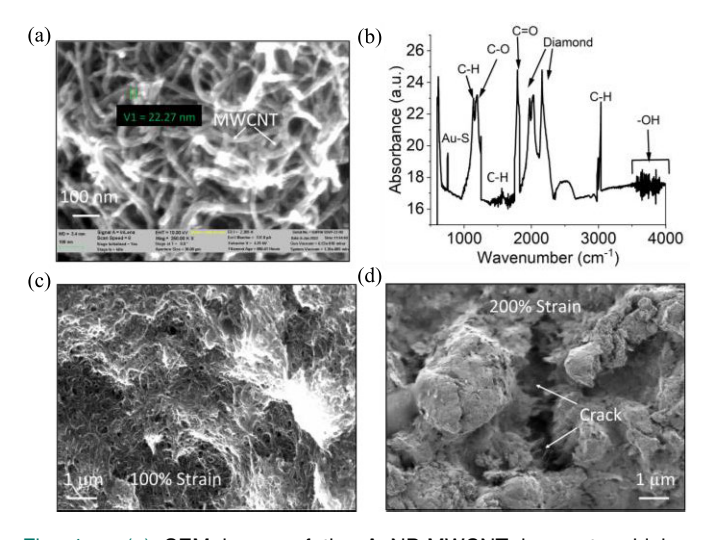


Fig. 4. (a) SEM image of the AuNP-MWCNT layer at a higher magnification to show the MWCNT fiber network and AuNPs (marked with green-colored text $V_1=22.27$ nm). (b) FTIR spectroscopy of AuNP-MWCNT. SEM images of AuNP-MWCNT-coated strain sensor after applying (c) 100% and (d) 200% of tensile strains. A homogenous MWCNT network is observed at 100% of tensile strain, whereas crack formation in the MWCNT network is visible when the sheet is stretched by 200%.

Furthermore, Fig. 4(c) and (d) shows the crack-free and cracked schematics of the MWCNT-coated strain sensor. Even under 100% of tensile strain, the SEM image shows a crack-free and homogenous MWCNT network [see Fig. 4(c)]. No noticeable structural deformation in the MWCNT network was observed at this strain value. However, beyond 180% (in this example, we applied a 200% of tensile strain) cracks started to form in the MWCNT network and underlying kirigami sheet, as shown in the SEM image of Fig. 4(d). The cracks created discontinuities in the conductive paths at several areas in the MWCNT network.

B. Sensor Calibration

We evaluated the strain sensing performance of the dual-functional device by applying varying bending and stretching strains and measuring the resistance variations with the data acquisition module shown in Fig. 3(c). The sensor was calibrated by mounting it on a motorized translation stage (MTS50-Z8, Thorlabs Inc., Newton, NJ, USA). Calibration was performed with sensors made on the 25- μ m kirigami substrate. As shown in Fig. 5(a), the AuNP-MWCNT layer exhibited a linear relative resistance ($\Delta R/R_0\%$) versus bending angle dependence. The sensitivity of a strain sensor is evaluated by the GF, which is defined as the ratio of relative change in sensor resistance to the mechanical strain

$$GF = \Delta R / R_0 / \Delta \varepsilon \tag{1}$$

where ΔR is the change in resistance from the initial value R_0 and ε is the applied bending strain defined by [49]

$$\varepsilon = \pm t/2r \tag{2}$$

where t is the thickness ($\approx 25 \ \mu m$) and r is the bending radius of the sensor. At a bending angle of 90° ($\Delta \varepsilon = 0.08\%$), the GF was 1.82. When the sensor was bent to 140° ($\Delta \varepsilon = 0.12\%$),

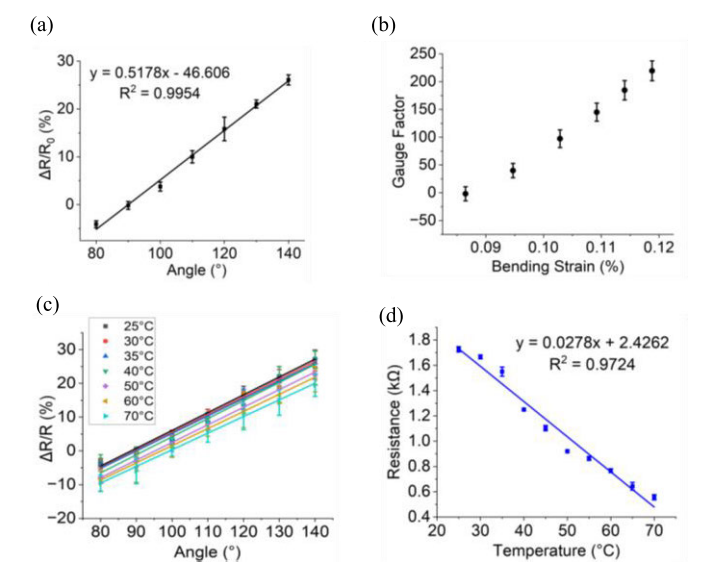


Fig. 5. (a) Response of the strain sensor under bending strain. (b) GF plot for the strain sensor. (c) Performance of the strain sensor at different temperatures. (d) Response of the temperature sensor under different temperatures. All measurements were repeated three times, where error bars represent the mean and standard deviation.

the GF became 219.54. The smallest angle and tensile strain detected by the sensor (also called limit of detection) were found to be approximately 0° and 2%, respectively. The GF in Fig. 5(b) is represented in terms of bending strain because this work demonstrates the application of the strain sensor in measuring angular deformations of different joints in the body (explained in Section IV).

In addition, the strain sensor was tested for different temperatures ranging from 25 °C to 70 °C, as shown in Fig. 5(c). For temperatures ranging from 25 °C to 40 °C, the sensor response showed a minimal deviation of 5%, which is acceptable considering the demonstrated application of the sensor in monitoring human body temperature (which ranges between 36.1 °C and 37.2 °C). Therefore, the temperature dependency of the strain sensor at higher temperatures will not affect the performance of the device when applied to the human body.

Likewise, the temperature sensor was calibrated for temperature values ranging from 25° to 70°. With increasing temperature, a decrease in the resistance of the AuNP-MWCNT layer was observed. The calibration curve in Fig. 5(d) exhibits a negative temperature coefficient of resistance for MWCNT, as was also observed in [50]. The temperature sensor had a sensitivity of $0.0278~\mathrm{k}\Omega/^\circ\mathrm{C}$.

C. Stretchability Analysis

The sensors were tested for stretchability by applying different amounts of tensile strain, as shown in Fig. 6(a) and (b). Two different thicknesses (25 and 125 μ m) of polyimide sheet were used to construct the kirigami patterned sensors. Fig. 6(a) shows the relative resistance of the graphene/AuNP-MWCNT-coated strain sensor fabricated on the two kirigami substrates in response to tensile strains ranging from 10% to 220%. In comparison to the planar polyimide sheet without any kirigami patterns, the kirigami-shaped strain sensors

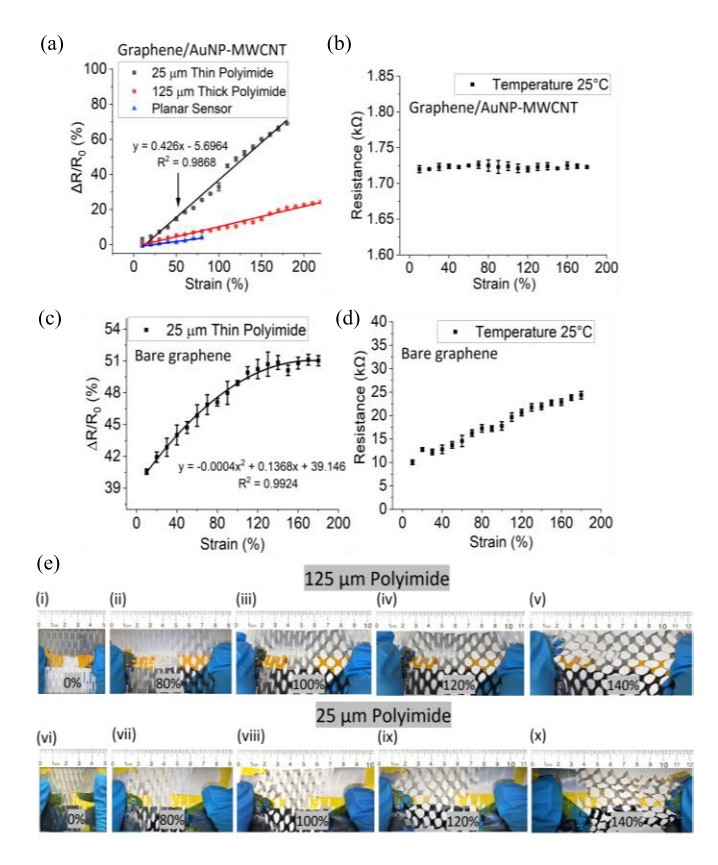


Fig. 6. (a) Relative resistance variations of the graphene/AuNP-MWCNT-coated strain sensor under different amounts of tensile strain. (b) Resistance variations of the graphene/AuNP-MWCNT-coated temperature sensor under different amounts of tensile strain. (c) Relative resistance variations of bare graphene-based strain sensor under different amounts of tensile strain. (d) Resistance variations of bare graphene-based temperature sensor under different amounts of tensile strain. All measurements were repeated three times, with the error bars representing the mean and standard deviation. (e) (i)–(v) 125- μ m kirigami substrate and (vi)–(x) 25- μ m kirigami substrate were each subjected to 80%, 100%, 120%, and 140% of stretching. The dimension changes are shown with respect to a ruler with unit in centimeters.

demonstrated a much higher sensitivity [as confirmed by the higher slope in Fig. 6(a)] to applied strain. The planar sensor lacked stretchability and could not undergo 3-D deformation due to the absence of kirigami patterns, thereby justifying the use of the kirigami framework in this work. Moreover, the strain sensor made on the 25- μ m-thick kirigami substrate demonstrated a higher sensitivity compared to the sensor made on the $125-\mu$ m-thick substrate. However, it is noteworthy that the $125-\mu m$ -thick substrate was functional and showed a reversible characteristic up to a maximum tensile strain of 220%, whereas the strain sensor on the 25- μ m kirigami sheet demonstrated a linear response to tensile strains up to 180%, beyond which cracks started to form. The cracks [as also shown in Fig. 4(d)] reduced the conductive paths in the MWCNT network, causing an increase in the resistance. Nevertheless, the 25- μ m kirigami substrate was chosen for its higher sensitivity. The response of the graphene/AuNP-MWCNT-coated temperature sensor made on the 25-µm kirigami substrate is shown in Fig. 6(b). Similar to the strain sensor, the temperature sensor also exhibited reliable performance up to 180% tensile strain. No noticeable variation in

TABLE I
RESPONSE OF THE SENSORS TO TORSION STRAINS

Torsion (°)	Relative Resistance of Strain Sensor (ΔR/R ₀ %)			
	25 μm Polyimide	125 µm Polyimide		
0	0.07±1.21	0.08±1.56		
180	58±2.74	22±3.65		
360	86±5.92	43±7.84		
Torsion (°)	Resistance of Temperature Sensor (R kΩ)			
	25 μm Polyimide	125 μm Polyimide		
0	1.72±0.004	1.68±0.54		
180	1.73±0.005	1.78±0.32		
360	1.74±0.004	1.85±0.67		

resistance was observed in response to stretching and releasing the kirigami substrate.

The relative resistance variations of the strain sensor [see Fig. 6(c)] and resistance variations of the temperature sensor [see Fig. 6(d)] under different amounts of tensile strain are characterized for bare graphene electrodes. Compared to the electrodes coated with graphene and AuNP-MWCNT, the bare graphene-based strain sensor exhibited a nonlinear response with a significantly lesser change in the relative resistance upon strain variations (resulting in a lower GF) [see Fig. 6(c)], while the bare graphene-based temperature sensor showed a high dependency on strain [see Fig. 6(d)], which are undesirable characteristics. Therefore, it is evident that AuNP-MWCNT-coated graphene exhibited an improved strain and temperature sensing performance under varied tensile strains.

Fig. 6(e) shows the structural deformations of the kirigami substrate upon stretching it by 80%, 100%, 120%, and 140%. The optical images further confirmed the high stretchability of the $25-\mu m$ kirigami substrate. Fig. 6(e) also shows the strain percentages measured with respect to a ruler. The kirigami designs initially deformed in-plane via the widening of cuts/hinges, followed by a rotation of the kirigami beams [51], [52].

Besides tensile and bending strains, the sensors were also subjected to torsional strains by twisting the opposite edges up to 180° and 360° [24]. Table I shows the responses (mean \pm standard deviation) of the sensors for five consecutive measurements at a fixed angle of rotation. It is evident that the strain sensor made on the $25-\mu$ m kirigami substrate showed higher sensitivity to the torsional strain. Moreover, the temperature sensor made on the $25-\mu$ m kirigami substrate experienced negligible strain (and hence a negligible variation in resistance) due to the combination of kirigami configuration and high flexibility of the thin substrate.

Therefore, we preferred a 25- μ m kirigami substrate due to its higher sensitivity, stretchability, and reversibility (discussed next), which are desired characteristics for precise monitoring of body movements.

D. Reversibility, Repeatability, Drift, and Washability Analyses

The *reversibility* test was conducted to confirm the reliable operation of the sensor when attached to different body parts.

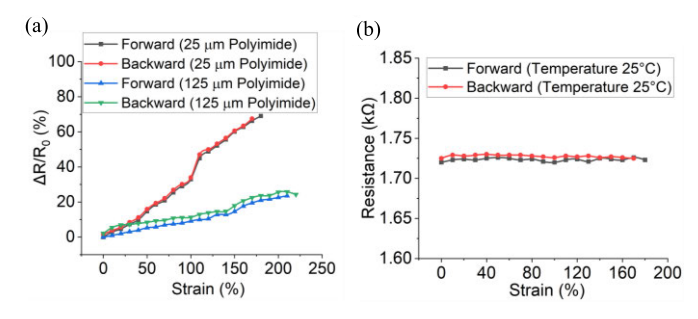


Fig. 7. Reversibility study where the kirigami substrates were subjected to 100 cycles of stretching and releasing at each strain value. Response of (a) strain and (b) temperature sensors.

Fig. 7(a) shows the response of the strain sensor upon stretching conditions. The experiment was conducted with sensors made on both 25- and 125- μ m-thick polyimide sheets cut into kirigami patterns. At a fixed strain value, $\Delta R/R_0$ remains consistent during 100 cycles of stretching and releasing. The "Forward" curve in Fig. 7(a) represents the response due to stretching the sheet only once, while the "Backward" curve corresponds to the response recorded after 100 cycles of stretching at each strain (%) value. There was no recovery time or lag time between the 100 cycles. The stretching cycles were carried out instantaneously. The 25-\(\mu\)m-thick kirigami substrate showed a smaller hysteresis (i.e., less than 5% between the zeroth and 100th cycles) compared to the 125-µm-thick sheet [see Fig. 7(a)]. Similarly, the temperature sensor was subjected to 100 cycles of tensile strain and the hysteresis was measured to be less than 5% [see Fig. 7(b)]. These results suggest the tensile recoverability and good durability of the sensors made on the 25- μ m-thick kirigami structure under repeated large strains. Hence, the 25- μ m-thick kirigami substrate was used in all dynamic experiments.

To characterize the *repeatability* of the sensors, three identical strain sensors were subjected to repeated bending (up to 100 cycles) at 90°, 120°, and 140° angles. The resulting responses of the three sensors are shown in Fig. 8(a). Similarly, the response of three identical temperature sensors was evaluated under 25 °C, 35 °C, and 40 °C [see Fig. 8(b)]. It is evident that both strain and temperature sensors demonstrate excellent repeatability with a negligible coefficient of variance of less than 2%.

The sensors were next evaluated for *drift* by measuring the sensor response over three days. Three identical sensors were used for drift analyses. The mean coefficient of variance was <3% and <2% for the strain [see Fig. 8(c)] and temperature sensors [see Fig. 8(d)], respectively, after three days, indicating the minimal drift displayed by the sensors.

For wearable sensors, the *washability* of the sensor is another important performance metric. Washability is particularly desired when the wearable sensor is integrated with the clothes that the user wears on a daily basis. To evaluate the washability of the kirigami sensors, the entire sheet was immersed in plain water, soap water, and isopropyl alcohol and subjected to shaking using an orbital shaker (ONiLAB, San Francisco, CA, USA) at 200 r/min. After approximately 1 h of washing and shaking, the sensors were dried at room

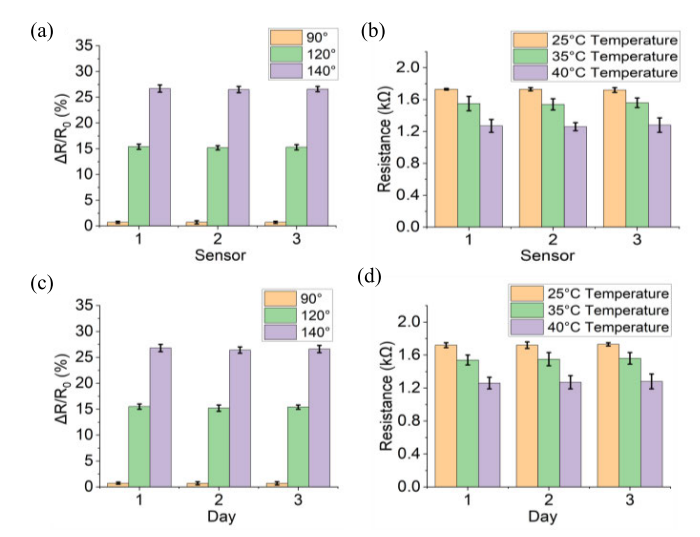


Fig. 8. Characterizing repeatability of (a) strain and (b) temperature sensors. Investigating the drift of (c) strain and (d) temperature sensors over three days. All measurements were repeated three times, with the error bars representing the mean and standard deviation.

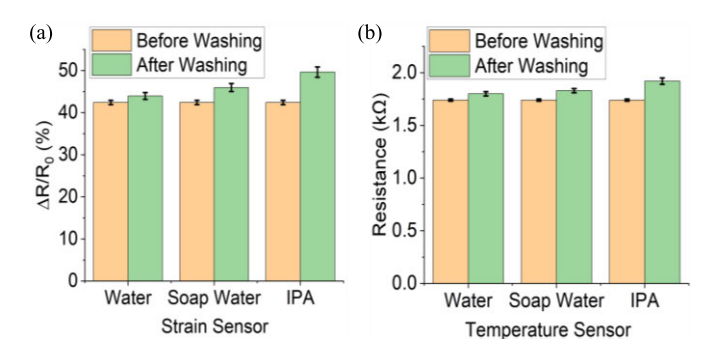


Fig. 9. Washability of the sensors in plain water, soap water, and isopropyl alcohol. Comparison of the response of (a) strain and (b) temperature sensors before and after washing for 1 h. All measurements were repeated three times, with the error bars representing the mean and standard deviation.

temperature, and the resistance measurements were recorded. No noticeable lamination of the sensor coatings from the polyimide substrate was observed after washing. As shown in Fig. 9, both the strain (in a relaxed position at 180°) and temperature (at 25 °C) sensors demonstrate no significant change in the response when washed with plain and soap water solutions, with a coefficient of variance found to be less than 4%, which was even smaller than what was observed in previous work [22]. Although the change in response was higher (approximately 10%) when the sensors were washed in isopropyl alcohol, clothes (embedded with sensors) are not generally washed in isopropyl alcohol.

Hence, we can summarize from the aforementioned results and discussion that our sensors demonstrate excellent reversibility, repeatability, drift performance, and washability, which are desired performance metrics for a wearable sensor.

IV. REAL-TIME SENSING PERFORMANCE A. Bending and Temperature Monitoring

The strain sensor could detect both bending and stretching deformations. This section deliberates the application of the

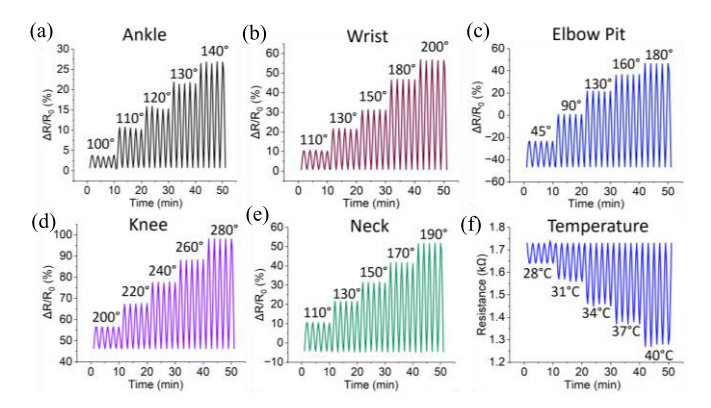


Fig. 10. Dynamic monitoring of the bending of (a) ankle, (b) wrist, (c) elbow pit, (d) knee, and (e) neck. (f) Dynamic response of the temperature sensor.

strain sensor in real-time bending monitoring. Fig. 10(a)–(e) shows the dynamic monitoring of the motions of the ankle, wrist, elbow pit, knee, and neck with the strain sensor, respectively. For this experiment, the sensor was attached between the leg and the foot to measure the bending motion of the ankle [see Fig. 10(a)], between the forearm and the hand to measure the bending motion of the wrist [see Fig. 10(b)], between the upper arm and the forearm to measure the bending motion of the elbow pit [see Fig. 10(c)], between the thigh and calf to measure the bending motion of the knee [see Fig. 10(d)], and between the thoracic and cervical spines to measure the bending motion of the neck [see Fig. 10(e)]. The placement of the sensor at different joints is shown in Fig. 11. The resistance responses were recorded under different amounts of bending. For instance, when the ankle was bent from 90° to 100°, 110°, 120°, 130°, and 140°, the mean relative resistance values were increased from 0.72% to 3.7%, 10.54%, 15.52%, 21.62%, and 26.68%, respectively. Similarly, bending motions of the wrist, elbow pit, knee, and neck were measured. The initial angle from which measurement started was 90°, 0°, 180°, and 80° for monitoring the bending of the wrist, elbow pit, knee, and neck, respectively. The strain sensor demonstrated excellent repeatability as was confirmed by the almost identical response upon repeated bending at each angle.

Furthermore, the temperature sensor was heated to different temperatures starting from the room temperature of 25 °C. Fig. 10(f) shows the dynamic response of the temperature sensor. The measurements of dynamic bending of different joints suggested excellent linearity between the relative resistance and the bending angle shown in Fig. 12(a)–(e). The temperature sensor also showed a linear response curve [see Fig. 12(f)]. All the measurements were carried out with the data acquisition and processing module shown in Fig. 3(c). The accuracy of the measurements computed with our processing unit was verified against the values recorded with an *LCR* meter.

B. Signal Decoupling

We evaluated the ability of the sensor to distinguish strain and temperature stimuli. The sensor was sequentially subjected to an individual temperature stimulus, an individual strain



Fig. 11. Placement of sensors at the joints in (a) ankle, (b) wrist, (c) elbow pit, (d) knee, and (e) neck.

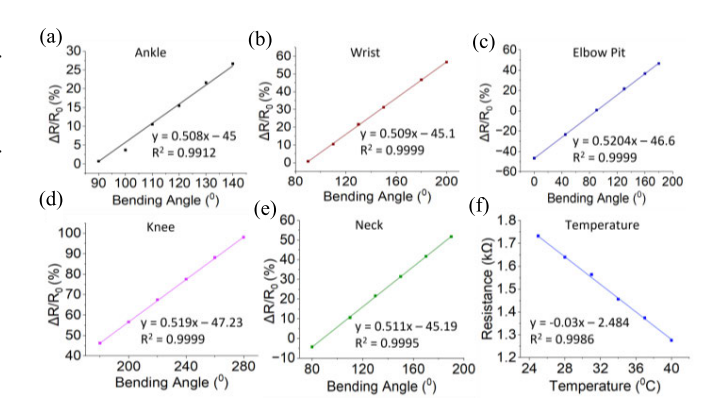


Fig. 12. Linear response of (a)–(e) strain and (f) temperature sensors.

stimulus, and a combined strain-temperature dual stimuli [22]. Fig. 13 shows the dynamic response of the sensors upon different combinations of applied stimuli. When the temperature was increased by 15 °C in the absence of any strain stimulus, only the resistance of the temperature sensor varied (Fig. 13(b) shows the absolute value of ΔR), whereas no change in the strain sensor response was detected [see Fig. 13(a)]. Although the same AuNP-MWCNT coating was used as both strain- and temperature-sensitive material, passivating the strain sensing electrodes with a thin layer of ecoflex protected the strain sensor from responding to fluctuations in temperature or other ambient parameters such as humidity. When the sensor was bent from 90° to 180°, only the strain sensor underwent a change in resistance [see Fig. 13(a)], while the temperature sensor did not show any noticeable change in its response. Upon stretching or bending, the strain applied to the temperature sensor was redistributed away from the sensor surface by the adjacent kirigami cuts and hinges. As a result, the temperature sensor encountered little to no changes in the

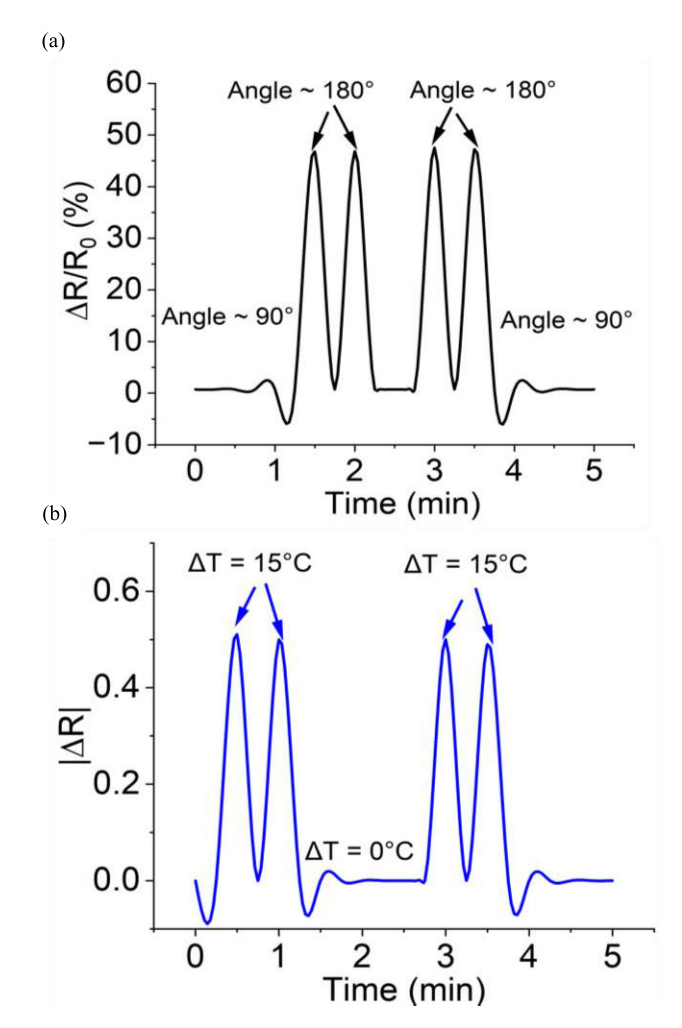


Fig. 13. Real-time monitoring of (a) bending strain and (b) temperature in response to a strain/temperature individual stimulus and strain-temperature coupled dual stimuli.

resistance upon motion artifacts (i.e., bending or stretching deformations of the kirigami structure). Thus, the underlying kirigami configuration enabled efficient decoupling of strain and temperature measurements. Finally, both temperature ($\Delta T = 15$ °C) and strain stimuli (bent to 180°) were applied. The responses to the dual stimuli were consistent with those produced under an individual temperature and strain stimulus.

The signal decoupling capability of the sensor makes it suitable for a wide variety of applications, including electronic skins, environmental monitoring, human–machine interfaces in robotic systems, and wearable healthcare.

C. Response Time

Further tests were conducted to evaluate the time taken by the sensors to reach a stable reading in response to a change in strain/temperature. As shown in Fig. 14, the strain sensor took almost 10 s to stabilize when the sheet was bent from 90° to 180°, while the temperature sensor took about 20 s upon increasing the temperature from 25 °C to 40 °C, indicating the fast response ability of the AuNP-MWCNT layer and the underlying kirigami structure. Delays of similar order were observed at other strain and temperature values.

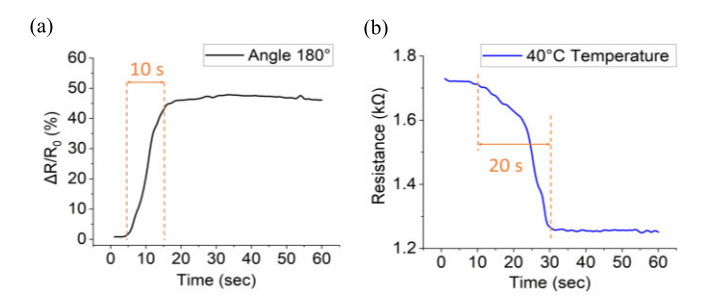


Fig. 14. Measurement of the dynamic response time of (a) strain and (b) temperature sensors.

TABLE II
PERFORMANCE COMPARISON OF FLEXIBLE STRAIN SENSORS

Coating Materials	Fabrication Technique	Gauge Factor	Max Strain (%)	Ref.
rGO/Elastic Tape	Stretching and releasing composite films	150	82	[53]
CNTs/Graphen e/PDMS	CVD/ catalytic growth/ pouring	0.36	20	[54]
GO/THF/ Ecoflex	Direct laser pattern	457	35	[55]
Graphene platelets/ MWCNT	Spray/ vacuum filtration method	181	7.5	[56]
Graphene/ Spandex/ Nylon Fabric	Scalable dip- reduce method	18.5	40.6	[57]
Graphene Foam/ Natural Rubber latex	Immersion and drying process	210	40	[58]
Graphene/Au NP-MWCNT/ Ecoflex	Screen printing	220	180	This Work

V. COMPARISON OF STRAIN SENSING PERFORMANCE

Table II provides a comparative analysis of our strain sensor with some notable strain sensors reported in the literature. The previously reported strain sensors listed in Table II were characterized for different types of bending movements, including finger bending, throat movements, and other body motions. However, these strain sensors were not characterized for specific bending angles, whereas our kirigami-patterned strain sensor was characterized for a wide range of bending angles from 0° to 280° on different body parts such as the ankle, wrist, elbow pit, knee, and neck. Moreover, our sensor demonstrates a higher GF and strain range compared to previously reported strain sensors outlined in Table II.

VI. CONCLUSION

In conclusion, this article reports a new type of kirigami-shaped hybrid sensing platform that measures both body movements and temperature. The kirigami architecture along with an ecoflex passivation layer allows the decoupling of sensor responses while simultaneously providing high stretchability, skin conformity, and repeatable sensing characteristics. The sensor was demonstrated to monitor bending deformations of different joints in the body. The sensor demonstrated excellent repeatability under different amounts of bending, stretching, and torsional strains. Hence, this

dual-functional sensor could find widespread applications in healthcare, haptics and interactive systems, tactile skin, soft sensors for soft robots and prosthetics, and environmental monitoring. In the future, the entire data acquisition system will be integrated into a single compact and flexible printed circuit board (PCB) so that no mobility or disconnection problems occur during the physiotherapy process.

ACKNOWLEDGMENT

The authors thank the applications specialists from Jeol, Inc., Peabody, MA, USA, and the Shimadzu Institute Nanotechnology Research Center, Arlington, TX, USA, for conducting SEM imaging of the sensors.

REFERENCES

- A. Mirelman et al., "Gait impairments in Parkinson's disease," *Lancet Neurol.*, vol. 18, no. 7, pp. 697–708, Jul. 2019, doi: 10.1016/S1474-4422(19)30044-4.
- [2] M. A. González-Gay, E. L. Matteson, and S. Castañeda, "Polymyalgia rheumatica," *Lancet Lond. Engl.*, vol. 390, no. 10103, pp. 1700–1712, Oct. 2017, doi: 10.1016/S0140-6736(17)31825-1.
- [3] P. Lorenzi et al., "Smart sensing systems for the detection of human motion disorders," *Proc. Eng.*, vol. 120, pp. 324–327, Jan. 2015, doi: 10.1016/j.proeng.2015.08.626.
- [4] R. Bootsman, P. Markopoulos, Q. Qi, Q. Wang, and A. A. Timmermans, "Wearable technology for posture monitoring at the workplace," *Int. J. Hum.-Comput. Stud.*, vol. 132, pp. 99–111, Dec. 2019, doi: 10.1016/j.ijhcs.2019.08.003.
- [5] S. Poitras, R. Blais, B. Swaine, and M. Rossignol, "Management of work-related low back pain: A population-based survey of physical therapists," *Phys. Therapy*, vol. 85, no. 11, pp. 1168–1181, Nov. 2005.
- [6] K. Lambers, D. Ootes, and D. Ring, "Incidence of patients with lower extremity injuries presenting to US emergency departments by anatomic region, disease category, and age," Clin. Orthopaedics Rel. Res., vol. 470, no. 1, pp. 284–290, Jan. 2012, doi: 10.1007/s11999-011-1982-z.
- [7] A. M. Gray and W. L. Buford, "Incidence of patients with knee strain and sprain occurring at sports or recreation venues and presenting to United States emergency departments," *J. Athletic Training*, vol. 50, no. 11, pp. 1190–1198, Nov. 2015, doi: 10.4085/1062-6050-50.11.06.
- [8] B. R. Waterman, B. D. Owens, S. Davey, M. A. Zacchilli, and P. J. Belmont, "The epidemiology of ankle sprains in the united states," *J. Bone Joint Surgery*, vol. 92, no. 13, pp. 2279–2284, Oct. 2010, doi: 10.2106/JBJS.I.01537.
- [9] B. R. Waterman, P. J. Belmont, K. L. Cameron, T. M. DeBerardino, and B. D. Owens, "Epidemiology of ankle sprain at the United States military academy," *Amer. J. Sports Med.*, vol. 38, no. 4, pp. 797–803, Apr. 2010, doi: 10.1177/0363546509350757.
- [10] C. Doherty, E. Delahunt, B. Caulfield, J. Hertel, J. Ryan, and C. Bleakley, "The incidence and prevalence of ankle sprain injury: A systematic review and meta-analysis of prospective epidemiological studies," *Sports Med.*, vol. 44, no. 1, pp. 123–140, Jan. 2014, doi: 10.1007/s40279-013-0102-5.
- [11] R. Elsoe, S. E. Ostgaard, and P. Larsen, "Population-based epidemiology of 9767 ankle fractures," *Foot Ankle Surgery*, vol. 24, no. 1, pp. 34–39, Feb. 2018, doi: 10.1016/j.fas.2016.11.002.
- [12] A. Mueller et al., "Continuous monitoring of patient mobility for 18 months using inertial sensors following traumatic knee injury: A case study," *Digit. Biomarkers*, vol. 2, no. 2, pp. 79–89, Aug. 2018, doi: 10.1159/000490919.
- [13] R. B. Roemer, "Engineering aspects of hyperthermia therapy," Ann. Rev. Biomed. Eng., vol. 1, pp. 347–376, 1999, doi: 10.1146/annurev.bioeng.1.1.347.
- [14] Q. Wang et al., "a skin-mountable hyperthermia patch based on metal nanofiber network with high transparency and low resistivity toward subcutaneous tumor treatment," Adv. Funct. Mater., vol. 32, no. 21, 2022, Art. no. 2270123, doi: 10.1002/adfm.202270123.
- [15] B. H. Dobkin and C. Martinez, "Wearable sensors to monitor, enable feedback, and measure outcomes of activity and practice," *Current Neu*rol. Neurosci. Rep., vol. 18, no. 12, p. 87, 2018, doi: 10.1007/s11910-018-0896-5.

- [16] M. O'Reilly, B. Caulfield, T. Ward, W. Johnston, and C. Doherty, "Wearable inertial sensor systems for lower limb exercise detection and evaluation: A systematic review," *Sports Med.*, vol. 48, no. 5, pp. 1221–1246, May 2018, doi: 10.1007/s40279-018-0878-4.
- [17] H. Tannous et al., "A new multi-sensor fusion scheme to improve the accuracy of knee flexion kinematics for functional rehabilitation movements," *Sensors*, vol. 16, no. 11, p. 1914, Nov. 2016, doi: 10.3390/s16111914.
- [18] Y.-P. Huang, Y.-Y. Liu, W.-H. Hsu, L.-J. Lai, and M. S. Lee, "Monitoring and assessment of rehabilitation progress on range of motion after total knee replacement by sensor-based system," *Sensors*, vol. 20, no. 6, p. 1703, Mar. 2020, doi: 10.3390/s20061703.
- [19] E. Akdoğan and M. A. Adli, "The design and control of a therapeutic exercise robot for lower limb rehabilitation: Physiotherabot," *Mechatronics*, vol. 21, no. 3, pp. 509–522, Apr. 2011, doi: 10.1016/j.mechatronics.2011.01.005.
- [20] X. Liao et al., "A highly stretchable ZnO@fiber-based multi-functional nanosensor for strain/temperature/UV detection," Adv. Funct. Mater., vol. 26, no. 18, pp. 3074–3081, May 2016, doi: 10.1002/adfm.201505223.
- [21] S. Bi, L. Hou, and Y. Lu, "An integrated wearable strain, temperature and humidity sensor for multifunctional monitoring," *Compos. A, Appl. Sci. Manuf.*, vol. 149, Oct. 2021, Art. no. 106504, doi: 10.1016/j.compositesa.2021.106504.
- [22] N. Wen et al., "Highly stretchable, breathable, and self-powered strain-temperature dual-functional sensors with laminated structure for health monitoring, hyperthermia, and physiotherapy applications," Adv. Electron. Mater., vol. 8, no. 11, Nov. 2022, Art. no. 2200680, doi: 10.1002/aelm.202200680.
- [23] P. Won et al., "Stretchable and transparent kirigami conductor of nanowire percolation network for electronic skin applications," *Nano Lett.*, vol. 19, no. 9, pp. 6087–6096, Sep. 2019, doi: 10.1021/acs.nanolett.9b02014.
- [24] T. Noushin, N. I. Hossain, and S. Tabassum, "Kirigami-patterned highly stable and strain insensitive sweat pH and temperature sensors for longterm wearable applications," in *Proc. IEEE Healthcare Innov. Point Care Technol. (HI-POCT)*, Mar. 2022, pp. 108–111, doi: 10.1109/HI-POCT54491.2022.9744070.
- [25] N. I. Hossain and S. Tabassum, "Performance analysis of a kirigamishaped temperature sensor," in *Proc. IEEE MetroCon*, Nov. 2022, pp. 1–3, doi: 10.1109/MetroCon56047.2022.9971137.
- [26] A. Lamoureux, K. Lee, M. Shlian, S. R. Forrest, and M. Shtein, "Dynamic kirigami structures for integrated solar tracking," *Nature Commun.*, vol. 6, no. 1, p. 8092, Sep. 2015, doi: 10.1038/ncomms9092.
- [27] R. Xu et al., "Kirigami-inspired, highly stretchable micro-supercapacitor patches fabricated by laser conversion and cutting," *Microsystems Nano-engineering*, vol. 4, no. 1, p. 36, Dec. 2018, doi: 10.1038/s41378-018-0036-z.
- [28] K. Yong, S. De, E. Y. Hsieh, J. Leem, N. R. Aluru, and S. Nam, "Kirigami-inspired strain-insensitive sensors based on atomicallythin materials," *Mater. Today*, vol. 34, pp. 58–65, Apr. 2020, doi: 10.1016/j.mattod.2019.08.013.
- [29] Y. Morikawa et al., "Ultrastretchable kirigami bioprobes," Adv. Healthc. Mater., vol. 7, no. 3, 2018, Art. no. 1701100, doi: 10.1002/adhm.201701100.
- [30] M. K. Blees et al., "Graphene kirigami," *Nature*, vol. 524, no. 7564, pp. 204–207, Aug. 2015, doi: 10.1038/nature14588.
- [31] L. Xu, X. Wang, Y. Kim, T. C. Shyu, J. Lyu, and N. A. Kotov, "Kirigami nanocomposites as wide-angle diffraction gratings," ACS Nano, vol. 10, no. 6, pp. 6156–6162, 2016, doi: 10.1021/acsnano.6b02096.
- [32] T. R. de Oliveira, W. T. Fonseca, G. de Oliveira Setti, and R. C. Faria, "Fast and flexible strategy to produce electrochemical paper-based analytical devices using a craft cutter printer to create wax barrier and screen-printed electrodes," *Talanta*, vol. 195, pp. 480–489, Apr. 2019, doi: 10.1016/j.talanta.2018.11.047.
- [33] J. Neto, R. Chirila, A. S. Dahiya, A. Christou, D. Shakthivel, and R. Dahiya, "Skin-inspired thermoreceptors-based electronic skin for biomimicking thermal pain reflexes," *Adv. Sci.*, vol. 9, no. 27, Sep. 2022, Art. no. 2201525, doi: 10.1002/advs.202201525.
- [34] Y. Yang and Z. D. Deng, "Stretchable sensors for environmental monitoring," Appl. Phys. Rev., vol. 6, no. 1, Mar. 2019, Art. no. 011309, doi: 10.1063/1.5085013.
- [35] Z. Li et al., "Real-time monitoring of plant stresses via chemiresistive profiling of leaf volatiles by a wearable sensor," *Matter*, vol. 4, no. 7, pp. 2553–2570, Jul. 2021, doi: 10.1016/j.matt.2021.06.009.

- [36] F. Liu, S. Deswal, A. Christou, Y. Sandamirskaya, M. Kaboli, and R. Dahiya, "Neuro-inspired electronic skin for robots," *Sci. Robot.*, vol. 7, no. 67, Jun. 2022, Art. no. eabl7344, doi: 10.1126/scirobotics.abl7344.
- [37] T. Noushin and S. Tabassum, "Kirigami-patterned IoT-enabled smart anklet to aid physiotherapy of patients with foot injury," in *Proc. IEEE Sensors*, Oct. 2022, pp. 1–4, doi: 10.1109/SEN-SORS52175.2022.9967128.
- [38] Z. Wang, L. Zhang, S. Duan, H. Jiang, J. Shen, and C. Li, "Kirigami-patterned highly stretchable conductors from flexible carbon nanotube-embedded polymer films," *J. Mater. Chem. C*, vol. 5, no. 34, pp. 8714–8722, 2017, doi: 10.1039/C7TC01727H.
- [39] B. Fasolt, M. Hodgins, G. Rizzello, and S. Seelecke, "Effect of screen printing parameters on sensor and actuator performance of dielectric elastomer (DE) membranes," Sens. Actuators A, Phys., vol. 265, pp. 10–19, Oct. 2017, doi: 10.1016/j.sna.2017.08.028.
- [40] T. Noushin, N. I. Hossain, and S. Tabassum, "IoT-enabled integrated smart wound sensor for multiplexed monitoring of inflammatory biomarkers at the wound site," *Frontiers Nanotechnol.*, vol. 4, Dec. 2022, Art. no. 851041, doi: 10.3389/fnano.2022.851041.
- [41] S. Seyedin et al., "Textile strain sensors: A review of the fabrication technologies, performance evaluation and applications," *Mater. Horizons*, vol. 6, pp. 219–249, Feb. 2019, doi: 10.1039/C8MH01062E.
- [42] J. R. Bautista-Quijano, P. Pötschke, H. Brünig, and G. Heinrich, "Strain sensing, electrical and mechanical properties of polycarbonate/multiwall carbon nanotube monofilament fibers fabricated by melt spinning," *Polymer*, vol. 82, pp. 181–189, Jan. 2016, doi: 10.1016/j.polymer.2015.11.030.
- [43] E. Bilotti, R. Zhang, H. Deng, M. Baxendale, and T. Peijs, "Fabrication and property prediction of conductive and strain sensing TPU/CNT nanocomposite fibres," *J. Mater. Chem.*, vol. 20, no. 42, pp. 9449–9455, Oct. 2010, doi: 10.1039/C0JM01827A.
- [44] J. Turkevich, P. C. Stevenson, and J. Hillier, "A study of the nucleation and growth processes in the synthesis of colloidal gold," *Discuss. Fara*day Soc., vol. 11, pp. 55–75, May 1951, doi: 10.1039/DF9511100055.
- [45] S. M. Vemuru, R. Wahi, S. Nagarajaiah, and P. M. Ajayan, "Strain sensing using a multiwalled carbon nanotube film," *J. Strain Anal. Eng. Design*, vol. 44, no. 7, pp. 555–562, Oct. 2009, doi: 10.1243/03093247JSA535.
- [46] O.-N. Hur, J.-H. Ha, and S.-H. Park, "Strain-sensing properties of multi-walled carbon nanotube/polydimethylsiloxane composites with different aspect ratio and filler contents," *Materials*, vol. 13, no. 11, p. 2431, May 2020, doi: 10.3390/ma13112431.
- [47] K. Xu, Y. Lu, S. Honda, T. Arie, S. Akita, and K. Takei, "Highly stable kirigami-structured stretchable strain sensors for perdurable wearable electronics," *J. Mater. Chem. C*, vol. 7, no. 31, pp. 9609–9617, Aug. 2019, doi: 10.1039/C9TC01874C.
- [48] A. Thamri, H. Baccar, C. Struzzi, C. Bittencourt, A. Abdelghani, and E. Llobet, "MHDA-functionalized multiwall carbon nanotubes for detecting non-aromatic VOCs," *Sci. Rep.*, vol. 6, no. 1, Oct. 2016, doi: 10.1038/srep35130.
- [49] S. Ke et al., "Screen-printed flexible strain sensors with Ag nanowires for intelligent and tamper-evident packaging applications," *Adv. Mater. Technol.*, vol. 5, no. 5, May 2020, Art. no. 1901097, doi: 10.1002/admt.201901097.
- [50] S. Lee, E.-M. Kim, and Y. Lim, "Near-zero temperature coefficient of resistance of hybrid resistor fabricated with carbon nanotube and metal alloy," *Sci. Rep.*, vol. 9, no. 1, p. 7763, May 2019, doi: 10.1038/s41598-019-44182-7.
- [51] D.-G. Hwang and M. D. Bartlett, "Tunable mechanical metamaterials through hybrid kirigami structures," *Sci. Rep.*, vol. 8, no. 1, p. 1, Feb. 2018, doi: 10.1038/s41598-018-21479-7.
- [52] A. Rafsanjani and K. Bertoldi, "Buckling-induced kirigami," *Phys. Rev. Lett.*, vol. 118, no. 8, Feb. 2017, Art. no. 084301, doi: 10.1103/Phys-RevLett.118.084301.
- [53] Q. Liu, J. Chen, Y. Li, and G. Shi, "High-performance strain sensors with fish-scale-like graphene-sensing layers for full-range detection of human motions," ACS Nano, vol. 10, no. 8, pp. 7901–7906, Aug. 2016, doi: 10.1021/acsnano.6b03813.
- [54] J. Shi et al., "Graphene reinforced carbon nanotube networks for wearable strain sensors," Adv. Funct. Mater., vol. 26, no. 13, pp. 2078–2084, Apr. 2016, doi: 10.1002/adfm.201504804.
- [55] L.-Q. Tao et al., "Self-adapted and tunable graphene strain sensors for detecting both subtle and large human motions," *Nanoscale*, vol. 9, no. 24, pp. 8266–8273, 2017, doi: 10.1039/C7NR01862B.

- [56] S. Lu et al., "Highly sensitive graphene platelets and multi-walled carbon nanotube-based flexible strain sensor for monitoring human joint bending," *Appl. Phys. A*, vol. 125, no. 7, p. 471, Jun. 2019, doi: 10.1007/s00339-019-2765-8.
- [57] H. Lee, M. J. Glasper, J. A. Nychka, J. Batcheller, H.-J. Chung, Y. Chen, and X. Li, "Preparation of fabric strain sensor based on graphene for human motion monitoring," *J. Mater. Sci.*, vol. 53, no. 12, pp. 9026–9033, 2018, doi: 10.1007/s10853-018-2194-7.
- [58] W. Zhang, B. Yin, J. Wang, A. Mohamed, and H. Jia, "Ultrasensitive and wearable strain sensors based on natural rubber/graphene foam," J. Alloys Compounds, vol. 785, pp. 1001–1008, May 2019, doi: 10.1016/j.jallcom.2019.01.294.



Tanzila Noushin (Student Member, IEEE) received the B.Sc. degree in electrical and electronics engineering from the Rajshahi University of Engineering and Technology (RUET), Rajshahi, Bangladesh, in 2016, and the M.S. degree in electrical engineering from The University of Texas at Tyler, Tyler, TX, USA, in 2022.

Her research interests include developing flexible and wearable sensors for biomedical applications.

Ms. Noushin has won several awards, including the University of Texas (UT) Tyler's 3-Minute Thesis Competition, the Student Employee Leadership Award, and the Third Place at Big Idea Pitch Competition in 2022 and 2021.



Shawana Tabassum (Member, IEEE) received the B.Sc. degree in electrical engineering from the Bangladesh University of Engineering and Technology, Dhaka, Bangladesh, in 2014, and the Ph.D. degree in electrical and computer engineering from lowa State University (ISU), Ames, IA, USA, in 2018.

From 2018 to 2020, she was a Postdoctoral Research Associate with Iowa State University. She is an Assistant Professor of Electrical Engineering with the University of Texas at Tyler,

Tyler, TX, USA, where she directs the Biosensors and Bioinformatics Laboratory. Her research focuses on the development of flexible, soft, and micro-/nano-structured optical and electrochemical sensors and actuators for biomedicine, and sustainable and precision agriculture.

Dr. Tabassum's notable awards and honors include the Curtis W. McGraw Research Award in 2023, the Mary John and Ralph Spence Professorship in 2023, the Dean's Award for Excellence in Research and Scholarship in 2022, the American Association of University Women's Research Publication Grant in 2022, the Science Breakthrough of the Year: Emerging Talent from the Falling Walls Lab Berlin Global Finale in 2020, the Robert J. Menges Award for Outstanding Research in Educational Development in 2020, the Postdoctoral Scholar Excellence Award for Teaching and Mentoring Students in 2020, the Best Global Impact Innovation Prize from the ISU's Pappajohn Center for Entrepreneurship in 2020 and 2019, the Biomedical Engineering Society's Career Development Award in 2019, the ISU's Research Excellence Award in 2018, and the Best Paper Award Finalist at the IEEE Sensors Conference in 2016.